The Journal of Adhesion, 78: 929–965, 2002

0021-8464/02 $12.00 +.00
DOI: 10.1080/00218460290010584

Taylor & Francis
Taylor & Francis Group

SURFACE ROUGHNESS EFFECTS ON MICROPARTICLE ADHESION

W. Cheng
P. F. Dunn
R. M. Brach
Particle Dynamics Laboratory, Department of Aerospace and Mechanical Engineering, University of Notre Dame, Notre Dame, Indiana, USA

A new self-consistent model is developed to treat the static contact of a microparticle with a flat barrier in the presence of molecular adhesion and surface roughness. Separation between their mean datum planes is modeled considering the elastic deformation of the microparticle and surface. The contact pressure is computed from the Lennard-Jones law following the Derjaguin approximation. The elastic deflection of the mean datum plane is calculated from the effective pressure by the half-space elastic theory. Roughness is modeled by introducing a Gaussian distribution to the gap between the surfaces. An effective pressure is defined as the statistical average of the contact pressure over the roughness heights. A solution satisfying all of the above conditions gives a self-consistent method of modeling adhesion between the microparticle and the flat barrier. Using collocation methods the equations are discretized as a large system of nonlinear algebraic equations. A continuation method is used to find the multiple numerical solutions for the mean separation and the effective contact pressure. Finally, adhesive contacts of both smooth and rough surfaces are simulated in a comparative manner to elucidate the features of surface roughness in the presence of molecular adhesion. The standard deviation of the Gaussian distribution is used as a parameter to assess the effects of roughness on the pull-off force. It is shown that increasing surface roughness significantly reduces the pull-off force and decreases the tendency for the microsphere to snap-on and snap-off.

Keywords: Microparticles; Adhesion; Contact forces; Surface roughness; Contact deformation; Snap-off

Received 8 November 2001; in final form 9 May 2002.

This research was supported in its early stage by the Center for Indoor Air Research (Contract No. 96-06) and the Electric Power Research Institute (Contract No. RP 8034-03).

Address correspondence to R. M. Brach, Department of Aerospace Engineering, Room 105 Hessert Center, University of Notre Dame, Notre Dame, IN 46556-5637, USA. E-mail: raymond.m.brach.1@nd.edu

INTRODUCTION

The modeling of microparticle adhesion has direct relevence to many engineering applications. Examples include those involving dry friction, fine particle agglomeration and separation, and microforce measurements such as those using the surface force apparatus, atomic force microscope, etc. [1]. More recent applications now can be found in Micro-Electro-Mechanical Systems (MEMS) and nanotechnology.

Adhesion between dry surfaces in contact with one another usually is modeled in continuum mechanics through the surface energy or the work of adhesion in separating adhering surfaces. Various adhesion models and hypotheses have been developed. These are summarized in the following in order to place the present study in proper context.

Modeling of Adhesion for Smooth Surfaces

As early as 1932, Bradley [2] found that the force of adhesion between two rigid spheres with radii R_1 and R_2 is $2\pi R\gamma$, where R is the equivalent radius $\frac{R_1R_2}{R_1+R_2}$ and γ is the combined surface energy, $\gamma = \gamma_1 + \gamma_2 - \gamma_1\gamma_2$. Derjaguin [3] found the same result from the Derjaguin approximation, assuming that the unit interaction energy between infinitesimal areas of solids is the same as the energy per unit area between half-infinite solids. For elastic spheres, two major models were developed, namely the JKR model [4] and the DMT model [5]. The JKR model modifies the Hertzian theory by considering the adhesion between surfaces within the contact region. The model was derived from the conservation of elastic energy, mechanical potential energy, and later using Griffith surface energy following a fracture mechanics approach. The DMT model assumed that adhesion acted outside the Hertzian contact region. The two models were seemingly contradictory until Tabor [6] suggested that they describe two opposite extremes of Tabor's parameter, μ. This parameter is the ratio of the elastic displacement of the surface at the point of separation (pull-off) to the effective range of surface forces characterized by the "equilibrium spacing," ϵ, at which intermolecular forces vanish:

$$\mu = \left(\frac{R\gamma^2}{E^2\epsilon^3}\right)^{1/3}. \tag{1}$$

E is the combined elastic modulus of the microparticles, where

$$\frac{1}{E} = \frac{1-\nu_1{}^2}{E_1} + \frac{1-\nu_2{}^2}{E_2}. \tag{2}$$

E_1 and E_2 are Young's modulus and ν_1 and ν_2 are the Poisson's ratios for the two contacting surfaces.

After Tabor's suggestion, Muller et al. [7] conducted a pioneering numerical simulation using a self-consistent model. Their model is termed "self-consistent" because the surface stress is coupled mathematically with the elastic deformation of the contacting surfaces. The surface tensile stress computed from the Lennard-Jones potential is used to calculate the elastic deformation of the surfaces. The surface deformation changes the molecular separation between surfaces, and the change of separation in turn changes the surface tensile stress according to the Lennard-Jones law. The solution considering all these factors satisfies both the Lennard-Jones law and the elastic deformation. The results of Muller et al. showed the continuous transition from the DMT model to the JKR model with increasing Tabor parameter values. This work was followed by a series of computational and analytical studies. Maugis [8] offered insight into the DMT-JKR transition through an analytical study using a Dugdale model. The Maugis-Dugdale theory gives an analytical description of the DMT-JKR transition. However, the Dugdale model is approximate in that it assumes that the surface force is a constant up to a maximum separation beyond which it decreases to zero. Multiple solutions are possible as long as they produce the same surface energy.

The Lennard-Jones model captures some unique features. Attard and Parker [9] performed a numerical study using the Lennard-Jones model. Unfortunately, because of a singularity in an integral, a nonmonotonic trend of pull-off force was found as Tabor's parameter was increased. The first detailed computation based on the Lennard-Jones model was done by Greenwood [10]. He repeated the computations done by Muller et al. [7] with more numerical accuracy and in greater detail. He found that the load-approach curves exhibited "S-shaped" inflections for values of Tabor's parameter larger than one, leading to snap-on and snap-off during contact. Recently, Feng [11] demonstrated a more reliable numerical method in finding multiple numerical solutions for the external load and displacement relationship. The snap-on and snap-off procedure during adhesive contact was described accurately. The studies of Muller et al. [7], Maugis [8], and Greenwood [10] collectively have led to a rigorous theory based on the self-consistent model using the Lennard-Jones force law and the half-space elastic deformation. Guided by these results, Johnson and Greenwood [12] constructed an adhesion map for the contact of elastic spheres showing valid regions for various adhesion models. It now is commonly accepted that the existing adhesion models for perfectly smooth elastic spheres can be set in the framework of two parameters

and one limit: the external load ratio, P, Tabor's parameter, μ, and the limit to remain in the elastic range. The magnitude of the pull-off force, P_c, varies from the DMT value, $2\pi\gamma R$, for $\mu < 0.1$ to the JKR value, $\frac{3}{2}\pi\gamma R$, for $\mu > 5$. The seemingly contradictory models have been shown to have a common basis using the Lennard-Jones law.

The Role of Surface Roughness

Even though adhesion is well described mathematically by a self-consistent model that couples the intermolecular forces with elastic deformation, the model is limited to smooth surfaces. It has long been realized that surface roughness significantly reduces adhesion in real contact (see Krupp [13], Sharpe [14], Tabor [6], and Johnson [15]). Effects on large spheres were observed and measured (see Fuller and Tabor [16]). Effects of roughness on adhesion have been observed in atomic force microscopy measurement (see Schaefer et al. [17], Mizes [18], Briscoe et al. [19], and Rabinovich et al. [20]) and in flow-induced particle detachment experiments (see Reeks et al. [21] and Soltani and Ahmadi [22]). Modeling of the effects of surface roughness is crucial in many problems. For example, in microparticle resuspension it has been realized that a rolling resistance model that does not consider surface roughness underestimates the microparticle detachment rate significantly. In order to match the experimental data, roughness effects must be included in the adhesion model (see Ingham and Yan [23] and Ziskind et al. [24]).

Existing adhesion models can be extended to consider rough surface contact. Rough surfaces are modeled by superposition of spherical asperities. Adhesive contact of a single asperity with a flat surface (or a large sphere) is modeled by the JKR or DMT theory. The adhesion of single asperities can be integrated to get the total adhesion force that results from multiple asperities (see Johnson [15], Ziskind et al. [24], Greenwood and Tripp [25] and Majumdar and Bhushan [26]). However, because of the nonlinearity of the problem, simple superposition may not be appropriate. Real adhesive contact with rough surfaces also involves overlapping contact areas due to neighboring asperities and possibly multiple snap-on and snap-off events for individual asperities. At present, it is impossible to include the effects of multiple snap-on and snap-off for each individual asperity summit. So, models based on single asperity contact are restricted to rough surfaces with sparse asperities such that single asperities are separated by long distances and do not interfere each other.

Computations in this paper are inspired by the pioneering work of Greenwood and Tripp [25] on pure elastic contacts of rough surfaces.

Greenwood and Tripp describe a rough surface as a series of hemispherical asperities with the same radii. The heights are assumed to follow a Gaussian distribution. Even though asperities on real surfaces can have any shape and any height distribution, there are reasons to justify their assumptions. According to the description of Greenwood and Williamson [27], there is a tendency for the heights to follow a Gaussian distribution about the mean surface. Studies also indicate that the essential behavior of elastic contact is determined primarily by the asperity height and secondarily by the shape of the asperities (see Greenwood [28]). By describing surface topology through probability distribution functions, the effects of roughness on elastic contacts can be analyzed statistically in a systematic manner.

This article presents a new method that introduces randomness to the pressure distribution of the self-consistent model of a single contact presented by Greenwood and Tripp [25] and later enhanced by Greenwood [10]. In the new model, instead of assuming multiple spherical asperities, the gap between a single contact of two spheres is perturbed with a statistical distribution that is a function of the contact radius. A Gaussian distribution is used in this paper, but others are possible. According to the Greenwood-Tripp model, separation between the mean datum planes of the contacting rough surfaces is computed by considering the elastic deformation caused by the contact pressure. With the statistical perturbation, an effective pressure is calculated as the statistical average of the Lennard-Jones forces over the random surface heights. Using collocation methods, the discrete governing equation becomes a large system of nonlinear algebraic equations. Then matrix-inverse-free path-following and pseudo arc-length methods are used to find multiple numerical solutions. Finally, both adhesive contacts of smooth and rough surfaces are simulated in a comparative manner to elucidate the salient features of surface roughness in the presence of molecular adhesion. The method generates detailed results on rough surface deformation and surface pressure during the contact. Results show that surface roughness can cause significant changes in the average properties of pull-off and in the status of snap-on and snap-off.

DESCRIPTION OF SURFACE ROUGHNESS

The first step in the modeling of rough surface adhesion is to define the surface roughness. It has been realized that surface complexity has a wide range of scales in height and spatial distributions. A rough surface can have a surface variation larger in size than the local contact spots, microscopic surface irregularities the same size as the contact

spots, and submicrometer and nanometer roughness, which has a scale much smaller than the contact spot or local asperity curvature. Therefore, real contact is a multiscale problem. Even if the tremendous computational difficulties can be handled, at present it still is impossible to include all scales to get meaningful conclusions.

This work considers a surface having submicrometer and nanometer-scale roughness. Effectively, the roughness scale is much smaller than the typical radii of micrometer-size particles. The roughness can be assumed to be spatially homogenous. Therefore, the relative shape of the rough microparticle and the rough flat barrier is described as a smooth sphere superposed with random perturbations (Johnson [29]). The smooth sphere denotes the mean datum plane and the random perturbations are refered to as roughness heights. Evidence shows that surface roughness heights follow a Gaussian distribution about the mean surface (see Greenwood and Williamson [27]). If the roughness height about the mean surface is s, then the probability distribution of s is

$$\phi(s) = \frac{1}{\sigma_s\sqrt{2\pi}} e^{-\frac{s^2}{2\sigma_s^2}}, \tag{3}$$

where σ_s^2 is the variance of roughness heights. Even though a Gaussian distribution is assumed, a real distribution can be used easily in the methods introduced in this paper. Using the above assumptions, an expression for the separation between two contacting spherical microparticles, or a microparticle and a flat barrier and its relationship with the statistical average contact pressure, can be derived.

THE MATHEMATICAL THEORY

According to the half-space theory, for a given axisymmetric normal surface traction, $p(\rho)$, the normal surface deflection, $w(\rho)$, can be estimated by the following equation (see Johnson [29]):

$$w(\rho) = \frac{4}{\pi E}\int_0^\infty \frac{t}{t+\rho} p(t)K(k)dt, \tag{4}$$

where ρ is the radial coordinate. Equation (4) is derived by assuming that surfaces are frictionless or made of similar material (the same assumption also is used for Hertzian theory). The combined elastic modulus, E, is defined in Equation (2). $K(k) = F(\frac{1}{2}\pi|k^2)$ is the complete elliptic integral of the first kind, and $k^2 = \frac{4t\rho}{(t+\rho)^2}$. In the present model, the contacting surfaces never really touch. The Lennard-Jones force

law is used to model the tensile stress, σ, between two bodies separated by a distance function, h (see Greenwood [10]):

$$\sigma(h) = \frac{8\gamma}{3\epsilon}\left[\left(\frac{\epsilon}{h}\right)^3 - \left(\frac{\epsilon}{h}\right)^9\right], \tag{5}$$

where ϵ is the spacing (at $\rho = 0$). Because $h = h(\rho)$, the stresses are distributed according to Equation (5). The Derjaguin approximation is used in the current model assuming that the Lennard-Jones law can be applied between infinitesimal areas of surfaces. Figure 1 shows the stress-separation relationship from the Lennard-Jones law. At the equilibrium spacing, $h = \epsilon$, the stress between two surfaces vanishes, so $\sigma = 0$. When the separation is smaller than the equilibrium spacing, $h < \epsilon$, there is a repulsive stress between the two surfaces and $\sigma > 0$. When the separation is larger than the equilibrium spacing, $h > \epsilon$, there is attractive stress and $\sigma < 0$. The maximum attractive stress is

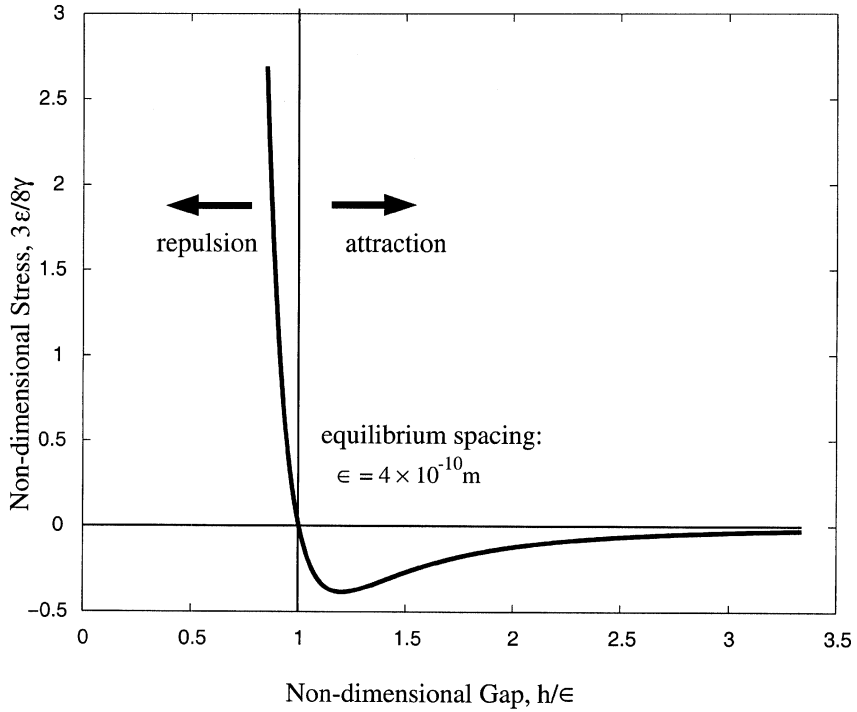

FIGURE 1 The stress-separation relationship according to the Lennard-Jones law.

$\frac{16\gamma}{9\sqrt{3}\epsilon}$ when the separation is $h = 3^{\frac{1}{6}}\epsilon$. The separation between two infinitesimal areas can never touch because $p \to \infty$ as $h \to 0$.

Assume that an elastic microparticle with radius R is in contact with the flat elastic barrier as shown in Figure 2 (R can also be a combined radius of curvature, $R = \frac{R_1 R_2}{R_1 + R_2}$, between the microparticle with radius R_1 and a curved surface with radius of curvature R_2). Because roughness is homogeneously distributed spatially, the separation, h, between two mean datum planes is axisymmetric as expressed in the following equation:

$$h(\rho) = -\alpha + \epsilon + \frac{\rho^2}{2R} + w(\rho), \tag{6}$$

where α is the mass center approaching distance between two microparticles, $\frac{\rho^2}{2R}$ is the combined surface height for a parabola with a

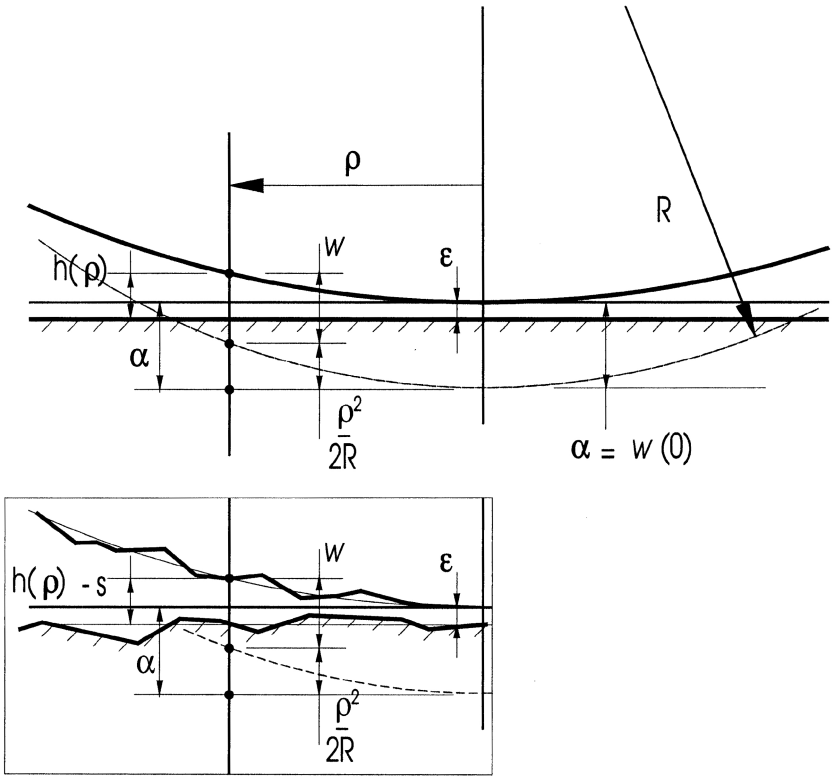

FIGURE 2 A microparticle in contact with a flat barrier.

combined radius R, and $w(\rho)$ is the elastic deflection of the mean datum plane. The expected value of the axisymmetric tensile stress, $p(\rho)$, from the Lennard-Jones law, can be estimated statistically as:

$$p(\rho) = \int_{-\infty}^{\infty} \sigma(h(\rho) - s)\phi(s)ds$$

$$= \frac{8\gamma}{3\sqrt{2\pi}\epsilon\sigma_s} \int_{-\infty}^{\infty} \left[\left(\frac{\epsilon}{h(\rho) - s} \right)^3 - \left(\frac{\epsilon}{h(\rho) - s} \right)^9 \right] e^{-\frac{s^2}{2\sigma_s^2}} ds. \qquad (7)$$

The problem is to find the pressure distribution $p(\rho) \equiv p^*(\rho)$ that satisfies Equations (4), (6), and (7). For convenience, the following dimensionless variables are introduced:

1. Separation: $H = h/\epsilon - 1$
2. Displacement: $W = w/\epsilon$
3. Approaching distance: $\lambda = \alpha/\epsilon$
4. Roughness height: $S = s/\epsilon$
5. Variance of roughness height: $\sigma_S^2 = \sigma_s^2/\epsilon^2$
6. Radial coordinate: $r = \rho/\sqrt{\epsilon R}$

Combining Equations (4), (6), and (7), the governing equation in the dimensionless form is:

$$H(r) + \lambda - \frac{r^2}{2} - \frac{32\mu^{3/2}}{3\sqrt{2\pi^3}\sigma_S} \int_0^{\infty} \frac{t}{t+r} K(k)$$

$$\times \int_{-\infty}^{\infty} \left[\frac{1}{[H(t) - S + 1]^9} - \frac{1}{[H(t) - S + 1]^3} \right] e^{-\frac{S^2}{2\sigma_S^2}} dS\, dt = 0, \qquad (8)$$

where μ is Tabor's parameter defined from the radius of curvature of the mean datum plane. For two microparticles or a microparticle and a flat barrier with the combined radius of curvature, R, the Tabor parameter is:

$$\mu \equiv \left[\frac{R\gamma^2}{E^2\epsilon^3} \right]^{1/3}. \qquad (9)$$

The Tabor parameter is a nondimensional quantity that includes the effects of surface energy per unit area, γ, microsphere radius, R, material elastic modulus, E, and interatomic spacing, ϵ. As the particle size or adhesion increases, the Tabor parameter increases. As the elasticity or interatomic spacing increases, the Tabor parameter

decreases. So, for example, a large flexible (soft) particle will have a large value of the Tabor parameter and a small, hard particle will have a small value of the Tabor parameter.

The dimensionless contact pressure is defined as:

$$P(r) = \frac{1}{\sqrt{2\pi}\sigma_S} \int_{-\infty}^{\infty} \left[\frac{1}{[H(r) - S + 1]^9} - \frac{1}{[H(r) - S + 1]^3} \right] e^{-\frac{S^2}{\sigma_S^2}} dS. \quad (10)$$

METHODS OF SOLUTION

Discretization

The effective pressure and the mean datum plane separation satisfying the elastic deflection and the Lennard-Jones law can be found numerically. The half-infinite domain, $r = [0, \infty]$, is approximated by a computational domain, $r = [0, r_m]$, with r_m large enough to give sufficient accuracy. The continuous physical domain for r is discretized into a finite number of elements. Element i corresponds to the subdomain confined between two neighboring nodes, $[r_i, r_{i+1}]$. The total number of nodes is N and the total number of elements is $N - 1$. To guarantee a smooth solution for the pressure, the separation is assumed to be linearly continuous on the nodes:

$$H = H_i \frac{r_{i+1} - r}{r_{i+1} - r_i} + H_{i+1} \frac{r - r_i}{r_{i+1} - r_i}. \quad (11)$$

Equation (8) can then be discretized in the computational domain. The residuals at the discrete nodes by the collocation method are:

$$G_i = H_i + \lambda - \frac{r_i^2}{2} - \frac{32\mu^{3/2}}{3\pi} \sum_{j=1}^{N} A_{ij} P_j. \quad (12)$$

P_j is evaluated by the Hermite integration. In the current study the 16-abscissa formula is used to achieve sufficient accuracy (see Abramowitz and Stegun [30]):

$$P_j = \frac{1}{\sqrt{2\pi}\sigma_S} \int_{-\infty}^{\infty} \left[\frac{1}{(H_j - S + 1)^9} - \frac{1}{(H_j - S + 1)^3} \right] e^{-S^2/\sigma_S^2} dS, \quad (13)$$

$$\approx \frac{1}{\sqrt{\pi}} \sum_{l=1}^{16} w_l \left[\left(\frac{1}{H_j - \sqrt{2}\sigma_S x_l + 1} \right)^9 - \left(\frac{1}{H_j - \sqrt{2}\sigma_S x_l + 1} \right)^3 \right]. \quad (14)$$

The influence matrix, A_{ij}, is a function only of the sizes of the elements, and can be calculated once for the collocation method. Special

treatment for singular elements and the numerical method for the elliptic integral of the first kind can be found in Feng [11]. The quantities x_l and w_l $(l = 1, 2, \ldots, 16)$ are the abscissas and weight factors for Hermite integration. The physical meaning of H_i is the separation between the mean datum planes of the two contacting surfaces at the ith grid node. By the collocation method, the residuals at grid nodes defined in Equation (12) are equal to zero. The unknowns, H_i, then are determined by solving the system of N equations, $G_i = 0$, $i = 1, 2, \ldots, N$.

Numerical Procedure

Solutions for Equation (12) are determined by two parameters: Tabor's parameter, μ, and the variance of the surface roughness heights, σ_S. For a given set of μ and σ_S, the separation vector, H, is a function of the approach distance, λ. Therefore, the nonlinear equation can be rewritten as a nonlinear eigenvalue problem:

$$G(H, \lambda) = 0, \quad G : R \times R^N \rightarrow R^N, \tag{15}$$

where $H = (H_1, H_2, \ldots, H_N)^T$ is the vector of unknowns and $G = (G_1, G_2, \ldots, G_N)^T$ is the vector of residuals. The solution path of Equation (15) can be found by the natural continuation method using λ as a natural continuation parameter. The initial point (H^0, λ^0) must be found at the beginning of the procedure. Usually, the extreme solution at a very large separation between the microparticle and the flat barrier ($\lambda \ll 0$) can be found easily and adopted as the initial point. The natural continuation method repeats two steps as illustrated in Figure 3:

- *predictor* step predicts a solution along the tangent of the solution path by linear extrapolation (or Taylor expansion); and
- *corrector* step finds a point approximately on the solution curve and close to the predicted point, in the current simulation, by Newton-Raphson steps (Press et al. [31]).

Suppose that the solution at the nth step (H^n, λ^n) has been found. The above two steps are used to find the solution (H^{n+1}, λ^{n+1}) at λ^{n+1}. In the predictor step, the tangent of the solution path at point (H^n, λ^n) is found first from the following equation:

$$G_H^n \phi_0 = -G_\lambda^n \tag{16}$$

and

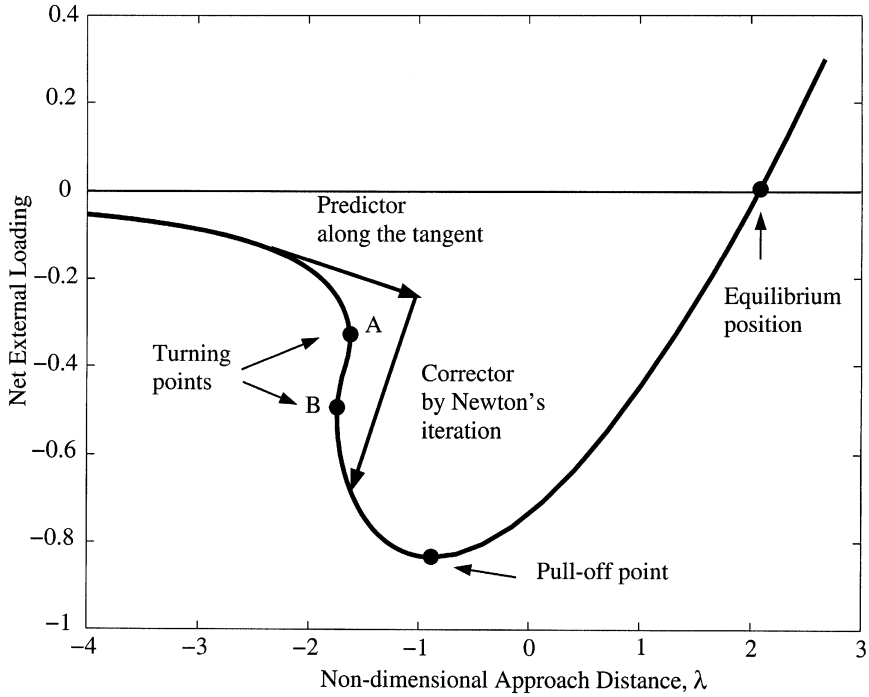

FIGURE 3 Illustration of the continuation method.

$$\dot{\boldsymbol{H}}^n = a\phi_0,\ \dot{\lambda}^n, \tag{17}$$

where a is determined from the following equation to normalize $(\dot{\boldsymbol{H}}^n, \dot{\lambda}^n)$:

$$a = \frac{\pm 1}{\sqrt{1 + ||\phi_0||^2}}. \tag{18}$$

If the sign of a is not properly chosen, either the iteration will be trapped at the same point or it will reverse the direction and compute the same path again. The sign of a must be chosen from the condition shown in the following equation (Keller [32]):

$$a[\dot{\boldsymbol{H}}^{T,n-1}\phi_0 + \dot{\lambda}^{n-1}] > 0. \tag{19}$$

With a step size Δ, an initial guess for the solution at $\lambda^{n+1} = \lambda^n + \Delta$ can be made from the extrapolation along the tangential direction:

$$H^{n+1} = H^n + \Delta \dot{H}^n. \tag{20}$$

In the corrector step, the Newton-Raphson method is used to find the accurate neighboring solution:

$$H^{n+1} = H^{n+1} + \delta H, \tag{21}$$

where δH is the solution of the linearized equation

$$G_H^{n+1} \delta H = -G^{n+1}, \tag{22}$$

where G_H is the Jacobian of the residual, G, to the separation, H:

$$G_H = \frac{\partial G}{\partial H}. \tag{23}$$

The Jacobian, G_H, is evaluated using the value of H derived in the previous iteration. The method has a quadratic convergence. The iteration stops when the relative error, $\delta H^T \delta H + (\delta \lambda)^2$, is less than a tolerance (10^{-15}).

In Equations (16) and (22) the inverse of the Jacobian, G_H, is needed when finding the tangent of the solution path and the correction terms for the Newton-Raphson iteration. Therefore, natural continuation works only for regular points at which the inverse of the Jacobian exists. However, λ involves an additional bifurcation parameter; multiple solutions may exist at certain values of λ. The points A and B shown in Figure 3 represent two turning points. They are simple singular points at which the Jacobian, G_H, is singular. Between points A and B, with the same value of λ, multiple solutions exist for H. The solution branch between A and B is unstable. The unstable solution can be used to explain the snap-on and snap-off behavior in adhesive contact. In order to find the whole solution path, including the unstable branch, a special technique to find solutions with a singular Jacobian is required. For a multiple solution problem such as this one, an addition parameter must be introduced to unfold the solution path about the turning points so that continuation methods can still be used. One possible parameter is the arc length. For the convenience of computation, a pseudo arc length is used instead when the value of the arc length is small. The main idea of pseudo arc length continuation is to drop the natural parameter, λ, and use the pseudo arc length as a new parameter to unfold the solution path. A calculated regular point on the solution path is (H^n, λ^n). The tangent of the solution path at this point is $(\dot{H}^n, \dot{\lambda}^n)$. The following equation describes a plane perpendicular to the tangent $(\dot{H}^n, \dot{\lambda}^n)$ at a distance Δ from (H^n, λ^n):

$$Q(H^{n+1}, \lambda^{n+1}, \Delta) = \dot{\boldsymbol{H}}^{T,n}(H^{n+1} - H^n) + \dot{\lambda}^n(\lambda^{n+1} - \lambda^n) - \Delta. \tag{24}$$

The plane described by Equation (24) intersects the solution path, Γ, if Δ and the curvature of Γ are not large. The intersection point is the solution for the next step. Using Newton's method, this leads to a new linear system:

$$\begin{pmatrix} G_H^n & G_\lambda^n \\ \dot{\boldsymbol{H}}^{T,n} & \dot{\lambda}^n \end{pmatrix} \begin{pmatrix} \delta H \\ \delta\lambda \end{pmatrix} = -\begin{pmatrix} G^n \\ Q^n \end{pmatrix}, \tag{25}$$

and the iterations are $H^{n+1} = H^n + \delta H$ and $\lambda^{n+1} = \lambda^n + \delta\lambda$. It is easy to prove that at the turning points G_H is singular but $\begin{pmatrix} G_H^n & G_\lambda^n \\ \dot{\boldsymbol{H}}^{T,n} & \dot{\lambda}^n \end{pmatrix}$ is not singular (see Keller [32]). Therefore, by introducing the equation for the pseudo arc length, turning points can be passed and the whole solution path can be found.

The natural continuation or pseudo arc length continuation steps are chosen depending on the value of $\dot{\lambda}$. Since $\dot{\lambda} = 0$ at the turning point, it is reasonable to switch to pseudo arc-length continuation when $\dot{\lambda} < 0.5$. Once the turning point is passed, $\dot{\lambda}$ increases again and the natural continuation is switched back.

To achieve an adequate accuracy, a large number of nodes is needed. Therefore, Equations (22) and (23) are large systems of linear equations. It is computationally unbearable in time to find their solutions by Gaussian elimination methods. A more efficient standard Generalized Minimum Residual (GMRES) iteration method is adopted instead. Because the inverse of the matrix is not needed in the GMRES method, the procedure is called a matrix inverse-free continuation method. The approach used in this paper is very efficient. The computation time for the whole solution path is in a PC time scale.

RESULTS AND COMPARISONS

Feng [11] showed that the upper limit of the computational domain, r_∞, can be set at 10 for smooth spherical contact. Results in the current study show that this value is also adequate for rough surface contact. To improve computational accuracy and efficiency, the nodes are unevenly distributed over the computational domain. The total number of evenly-distributed nodes are $N_e = 501$. Extra nodes are added near the regions where H and P change significantly. The total number of nodes for most cases is $N = 531$. Both smooth and rough contacts are simulated in a comparative manner to elucidate the

salient features of surface roughness in the presence of molecular adhesion.

Results for Smooth Surfaces

The dimensionless net external load, F, is defined by the equation

$$F = \frac{8}{3}\int_0^{r_\infty} P(r) r\, dr. \tag{26}$$

A positive value of F corresponds to compression and a negative value of F corresponds to attraction. Figure 4 shows the computed load-approach relationship for small Tabor parameter values ($\mu < 1.0$). Each value of λ corresponds to one external force. In other words, the external force can be measured by the approaching distance. However, the load-approach relationship is not monotonic and cannot be measured by the external force. In microparticle attachment, when two

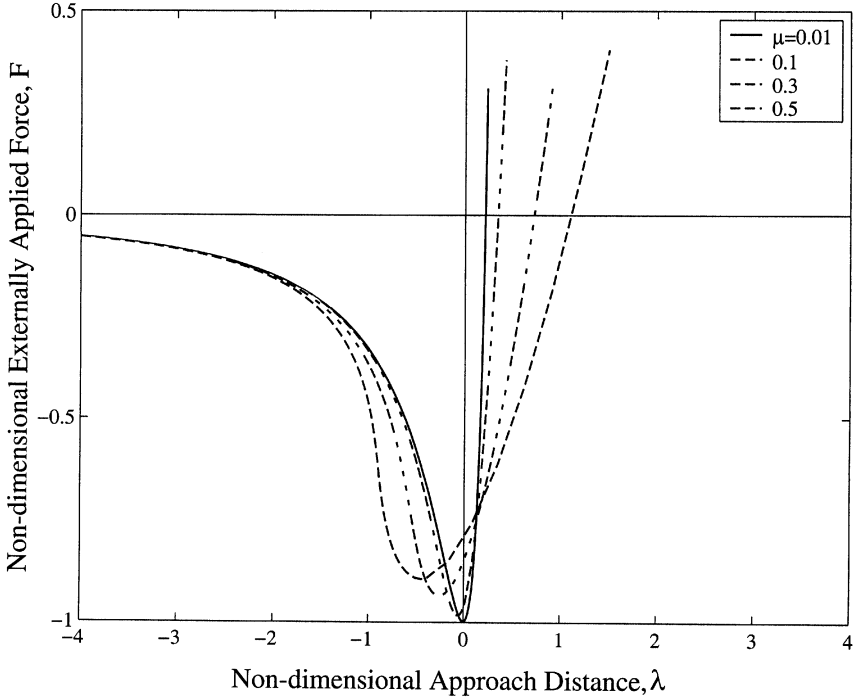

FIGURE 4 The load-approach curves for $\mu = 0.01$, 0.1, 0.3, and 0.5 for smooth surfaces.

surfaces are separated by a relatively large distance ($\lambda \ll 0$) the net external load is attraction. The attraction and the approach increase when the surfaces become closer. The attraction force reaches its peak at a certain distance, λ_p. The force, F_p, at $\lambda = \lambda_p$ is defined as the pull-off force. For very small Tabor parameter values ($\mu < 0.1$), λ_p is near zero. The value of λ_p decreases when μ increases. The pull-off force for small Tabor parameter values is approximately equal to 1 scaled by $2\pi\gamma R$, which is the value from the DMT theory. An extreme case is when $\mu = 0$, for which the pull-off force and the corresponding separation can be found directly according to Equation (8)

$$H(r) = -\lambda + \frac{r^2}{2} = 0. \tag{27}$$

Substituting Equation (27) into Equations (26) and (10) gives the following expression for the external force as $\mu = 0$ (see Feng [11]):

$$F = \frac{1 - 4(1-\lambda)^6}{3(1-\lambda)^8}. \tag{28}$$

Thus, for $\mu = 0$ the pull-off force is -1 at $\lambda_p = 0$. Figure 4 shows that when μ is very small the solution on F_p and λ_p agrees with the asymptotical solution for $\mu = 0$. When the approach increases further, the external force begins to increase again. At the equilibrium position, which corresponds to the approach, λ_e, the net external force vanishes. The equilibrium approach distance for $\mu = 0$ is $\lambda_e = 1 - 2^{-1/3}$ from Equation (28). The equilibrium approach for $\mu = 0.01$ is approximately 0.206, which is very close to the value for $\mu = 0$. When the contacting surfaces approach each other further ($\lambda > \lambda_e$), the net external force changes to compression ($F > 0$) and increases rapidly because of elastic deformation and the Lennard-Jones model. The effect of intermolecular adhesion becomes more significant when $\mu \geq 1.0$.

The snap-on and snap-off process exists as discussed by Attard and Parker [9], Greenwood [10], and recently by Feng [11]. As shown in Figure 5 on the curve of $\mu = 1.0$, there are two special points, A and B, at $\lambda_a = -1.74$ and $\lambda_b = -1.63$, respectively. The values of the slope at A and B are ∞ and the Jacobians at A and B are singular. Points A and B are turning points because the stability of the solution changes around these two points. In the interval of $-1.74 \leq \lambda \leq -1.63$, three branches of solutions for the separation, $H(r)$, and the contact pressure, $P(r)$, exist. The branch between points A and B is unstable and the other two branches are stable, as shown in Figure 5.

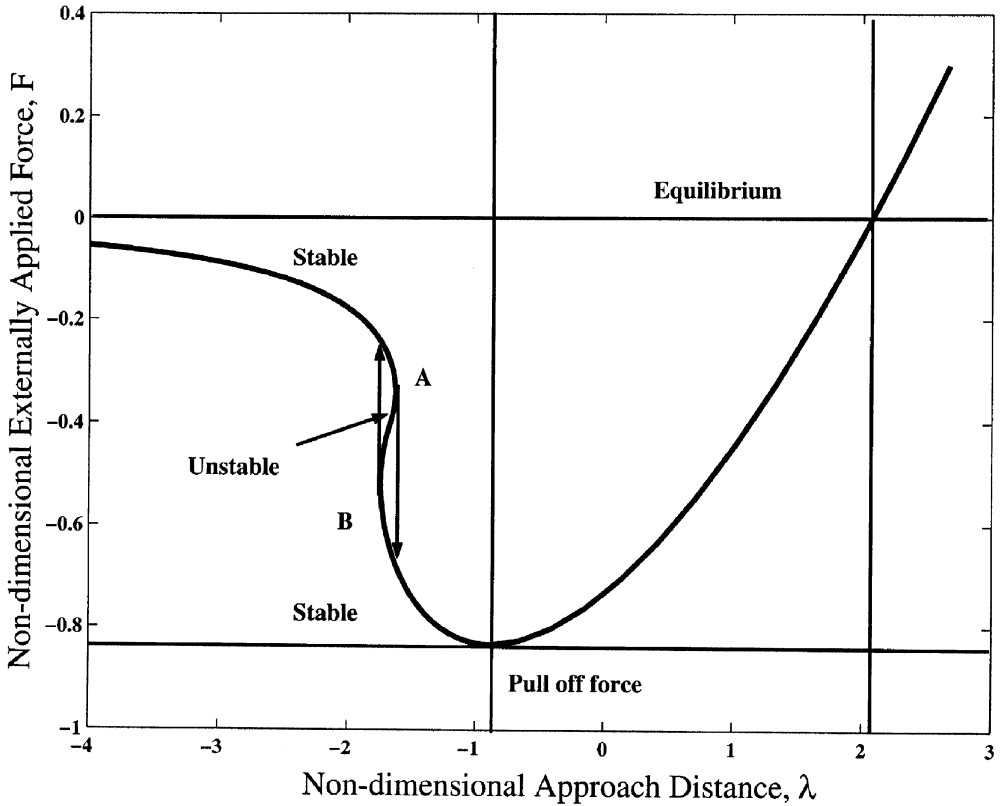

FIGURE 5 The load-approach curves for $\mu = 1.0$ for smooth surfaces.

In microparticle attachment, F decreases continuously during approach as λ increases (the two surfaces become closer). At $\lambda = \lambda_a$ (point A), because solutions between points A and B are unstable, the solution falls to the lower stable branch. This phenomenon is called "snap-on," and point A is called the snap-on point. The theory followed here is static; inertia does not play a role and the external force decreases instantaneously. Figure 6 shows the profiles of separation and surface stress just before and just after snap-on. Just before snap-on, the whole profile of the surface stress is attraction. There is no significant change in the profile of separation. After the instability, the stress in the contact area reduces and the separation over the contact region is relatively flat as shown in Figure 6. The slope of the separation at the edge of contact changes significantly. The peak of attraction stress moves from the center to the periphery of the contact region. The location of the peak of the stress is the same as the location of a significant change in the slope of the separation profile. Therefore, the edge of contact can be located as the center of the peak of the attractive stress, as shown in Figure 6.

In detachment, the approach decreases from the equilibrium position ($\lambda = \lambda_e$) to the turning point B (Figure 5) by passing the attraction peak, P. At $\lambda = \lambda_b$, the solution jumps to the stable branch and the external force increases suddenly toward zero. In Figure 7, just before snap-off, negative attractions concentrate on the periphery of the contact region. At point B, microparticles snap-off and contact is lost. The peak of the surface stress relocates to the center at $r = 0$. When $\mu \geq 1.0$, at least one snap-on and one snap-off point exist as shown in Figure 8. When $\mu \geq 5.0$, secondary turning points appear due to strong intermolecular attraction. Figure 9 shows the secondary snap-on and snap-off in detail for $\mu \geq 2$.

The strong intermolecular force also affects the value of the pull-off force. Figure 8 shows that the pull-off force for $\mu \geq 5.0$ is near the JKR value, $\frac{3}{2}\pi R\gamma$. JKR theory is the extreme case for large Tabor parameter values. Figure 10 shows the profile of separation and surface stress at the pull-off position for $\mu = 0.01$ and 3.0. When the Tabor parameter value is large ($\mu \geq 1.0$), the attractive stress concentrates at the edge of the contact area. The slope of the attractive stress changes sharply and the attractive stress decays suddenly near the edge of the contact area. When μ is very large, the solution approaches the asymptotic solution from the JKR theory. The stress is not as concentrated and the slope of separation does not change as rapidly at the edge of contact such as for the case of $\mu = 0.01$. Therefore, the JKR theory is not accurate for small Tabor parameter values and the DMT theory is more suitable.

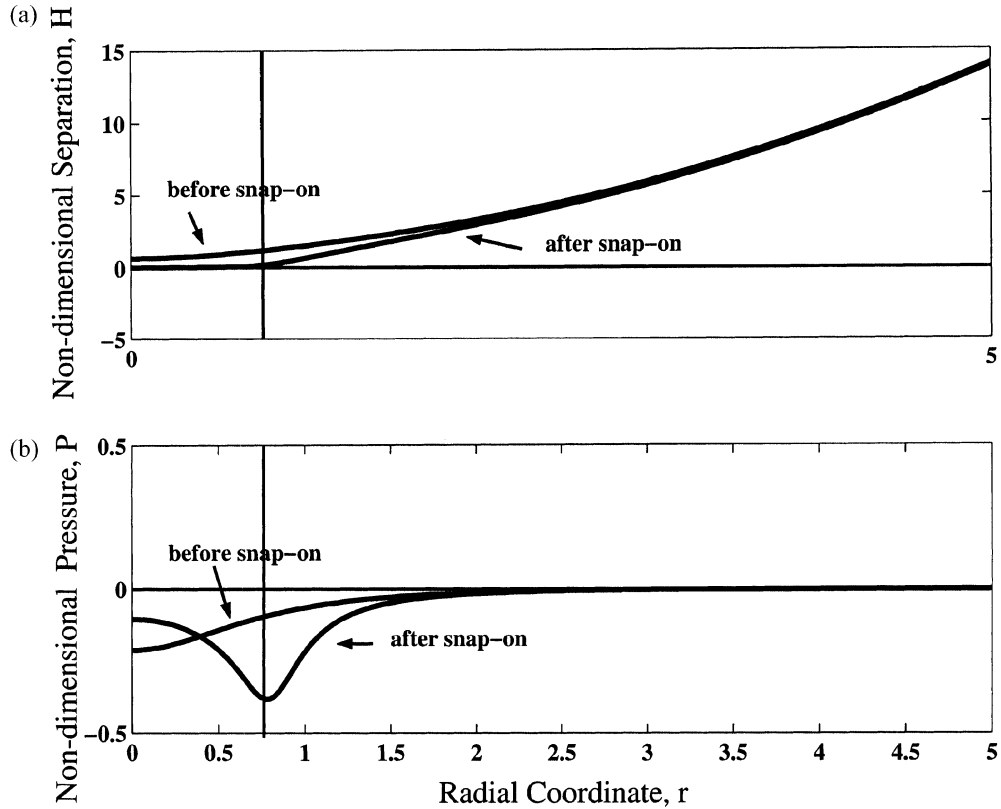

FIGURE 6 The profiles of surface stress and separation before and after snap-on for $\mu = 1$.

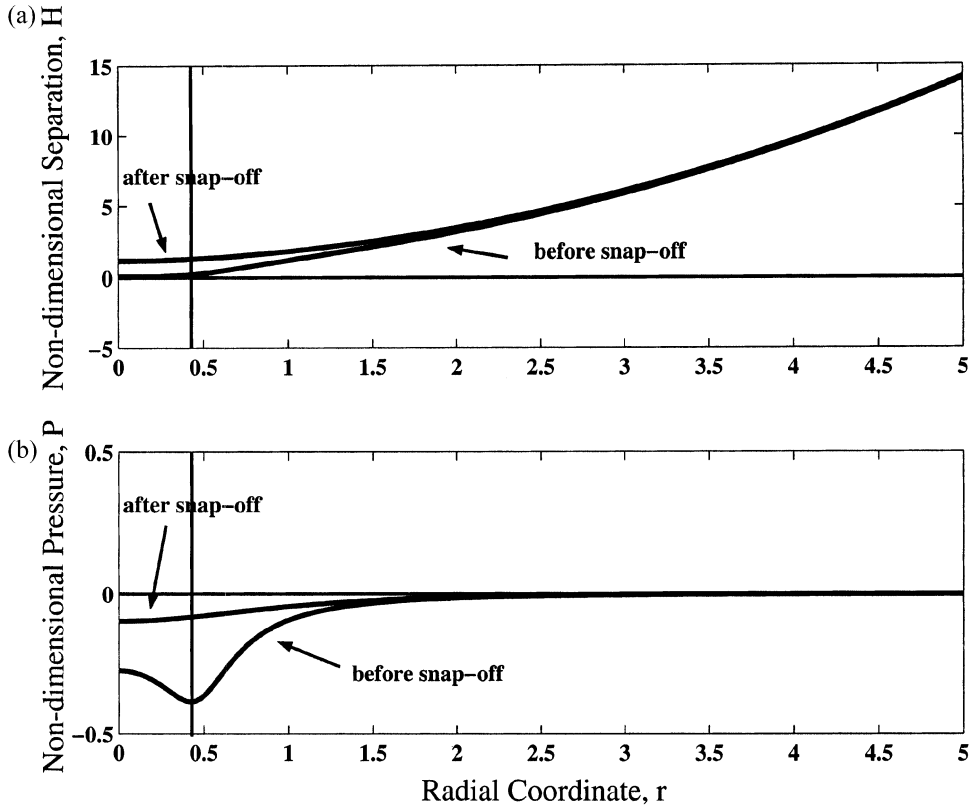

FIGURE 7 The profiles of surface stress and separation before and after snap-off for $\mu = 1$.

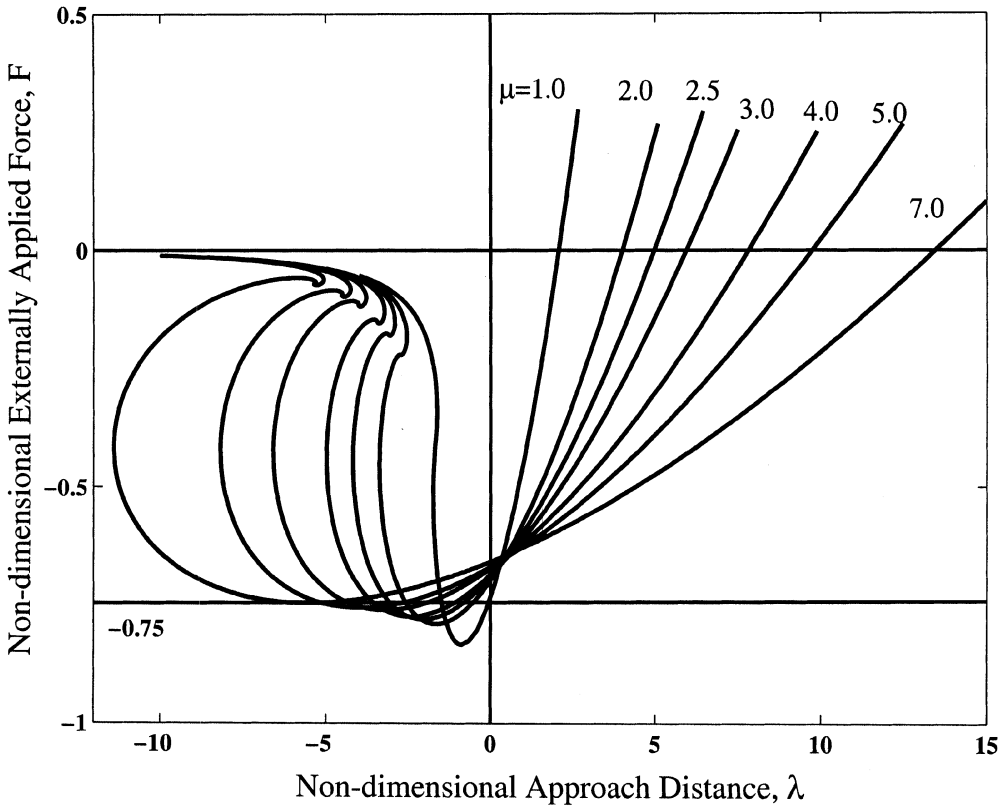

FIGURE 8 The load-approach curves for $\mu = 1.0, 2.0, 2.5, 3.0, 4.0, 5.0$, and 7.0 and details near the turning points.

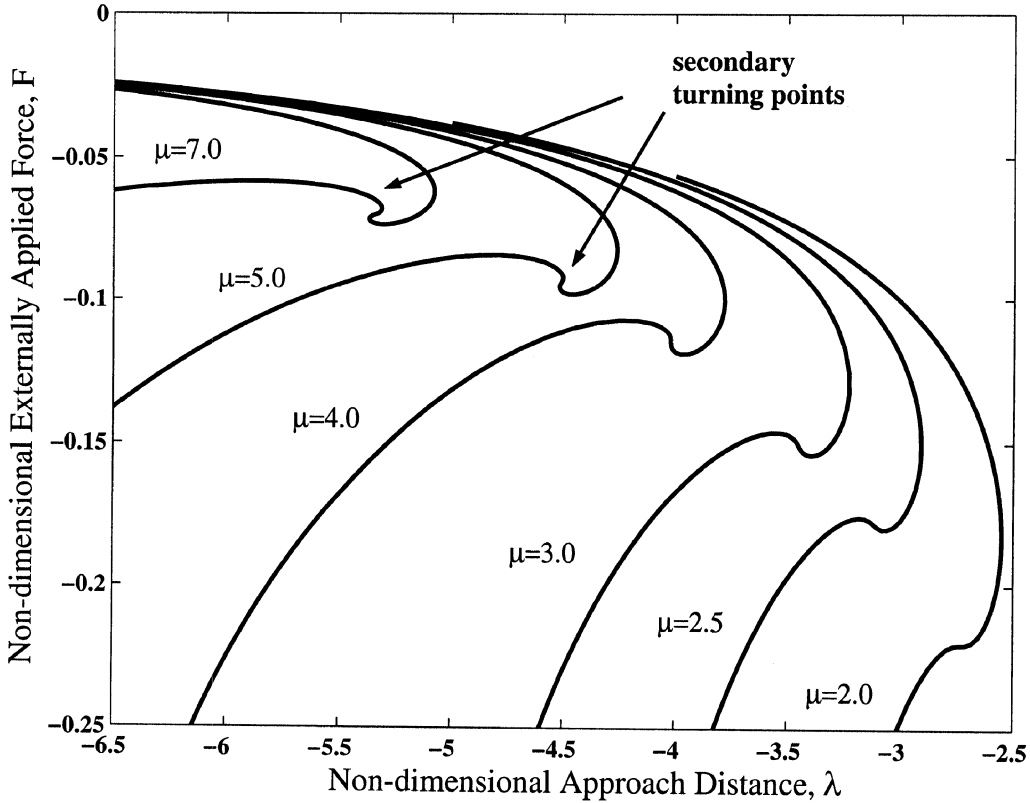

FIGURE 9 The details near the turning points of the load-approach curves for $\mu = 2.0, 2.5, 3.0, 4.0, 5.0$, and 7.0.

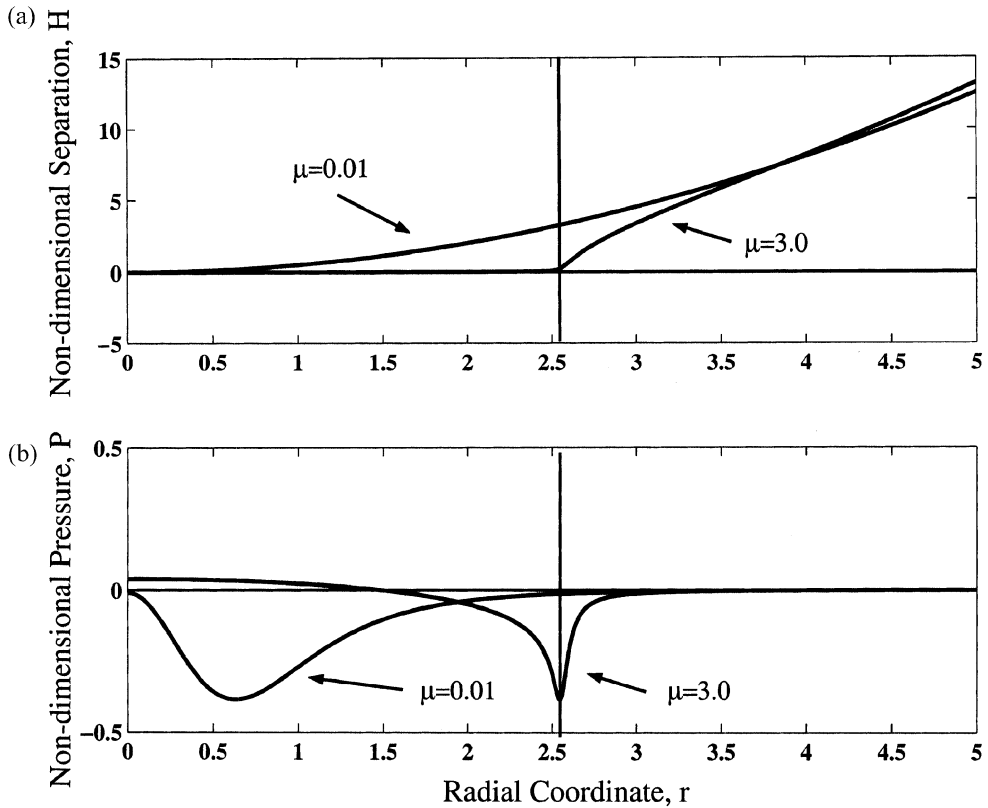

FIGURE 10 Profiles of separation and surface stress at the pull-off position for $\mu = 0.01$ and $\mu = 3.0$.

Another important feature affected by the Tabor parameter is the equilibrium position at which the external force vanishes ($F = 0$). According to the computation results shown in Figure 8, the equilibrium positions are $\lambda_e = 2.07$ and 13.44 for $\mu = 1.0$ and $\mu = 7.0$, respectively. With an increase in the value of the Tabor parameter the approach distance at the static equilibrium, λ_e, increases significantly. This indicates that when the Tabor parameter is large (corresponding to a large, soft microparticle with a flat barrier), the microparticle is highly deformed at the static equilibrium state. Figure 11 shows the profile of separation and surface stress for $\mu = 0.01$ and $\mu = 3.0$ at the equilibrium position. It clearly reveals that at the equilibrium position the microparticle is deformed more significantly with a larger contact radius when $\mu = 3.0$. Even though in both cases the net external loads are zero, because of a higher elasticity a small deformation corresponds to a higher contact pressure. Therefore, the case of $\mu = 0.01$ has a stronger repulsive stress. The deformation of the microparticle is more significant for larger Tabor parameter values.

The effect of the value of the Tabor parameter can be observed also from the separation and surface stress profile at $\lambda = 0$. Figure 12 shows the profile of separation and tensile stress for $\mu = 0.01$ and 3.0 at $\lambda = 0$. There is little deformation for $\mu = 0.01$ but obvious deformation for $\mu = 3.0$. It demonstrates clearly that the change of the slope of the attractive stress and the separation at the edge of the contact is sharper for higher Tabor parameter values.

Effects of Surface Roughness on Microparticle Adhesion

As shown by the governing equations, the microparticle adhesion considering surface roughness is determined not only by the value of Tabor's parameter but also by the variance of the roughness heights. The effects of various Tabor's parameter values have been demonstrated previously for smooth surfaces. This section focuses on the effects of surface roughness on microparticle adhesion. To understand more easily the effect of surface roughness, we define the reduction rate of the pull-off force, ϕ_r, as

$$\phi_r = 1 - \frac{F_p}{F_{p0}}, \tag{29}$$

where F_p is the pull-off force for a rough surface and F_{p0} is the pull-off force for a smooth surface.

Figure 13 shows the load-approach curves for $\mu = 0.01$ for Gaussian surface roughness. The pull-off force for a smooth surface

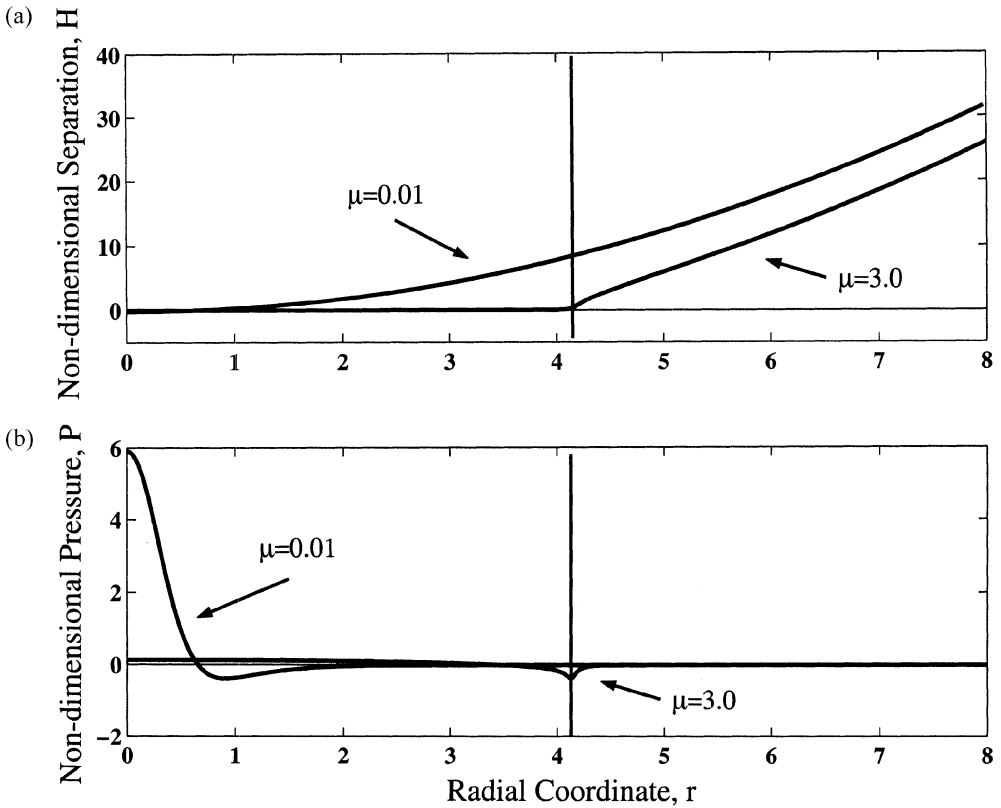

FIGURE 11 Profiles of separation and surface stress for $\mu = 0.01$ and $\mu = 3.0$ at the equilibrium position.

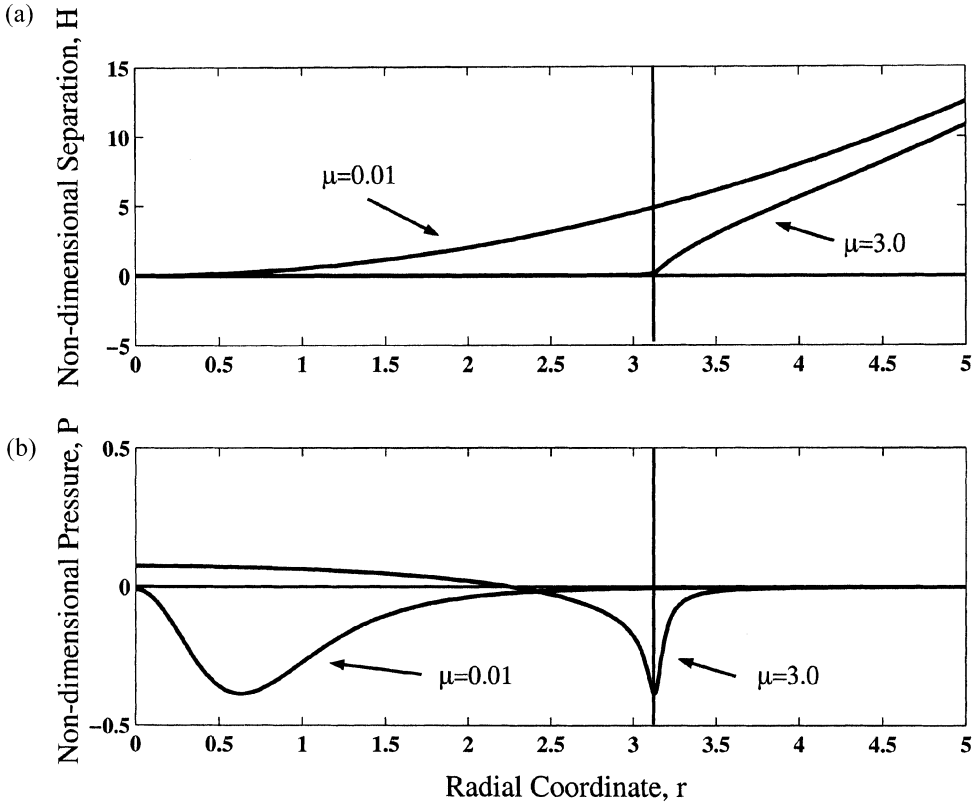

FIGURE 12 Profiles of separation and surface stress for $\mu = 0.01$ and $\mu = 3.0$ at $\lambda = 0$.

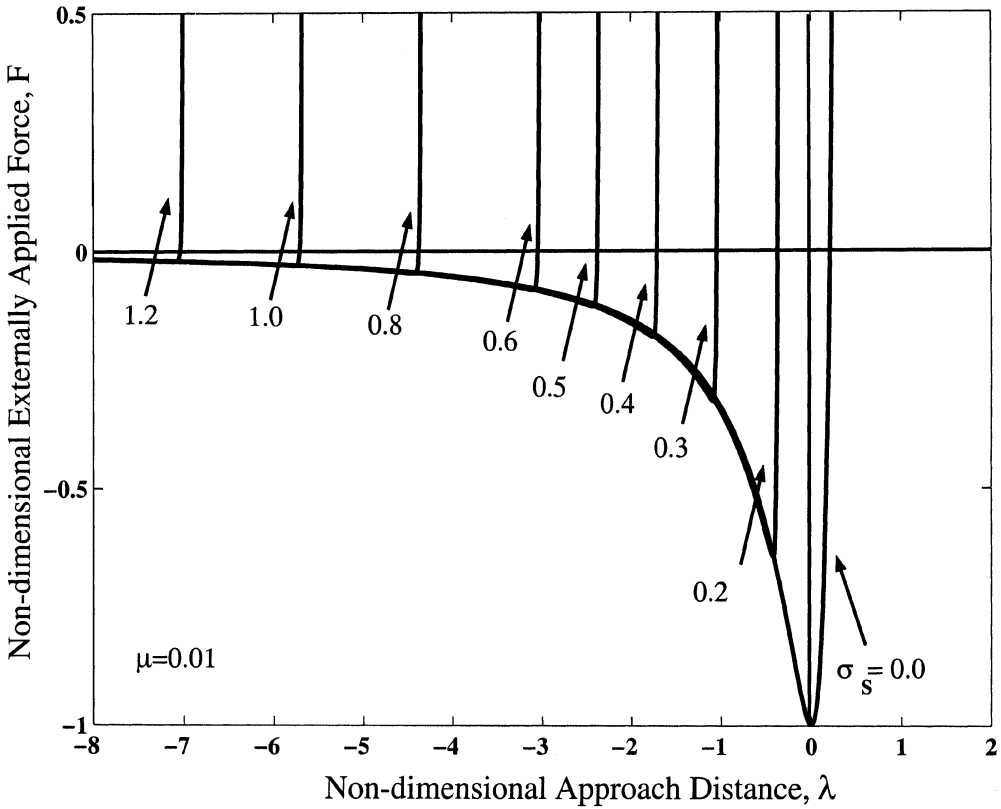

FIGURE 13 Load-approach curves for $\mu = 0.01$.

($\sigma_S = 0$) is $F_p = -1$ (the DMT value). Surface roughness reduces the pull-off force dramatically. For example, for $\sigma_S = 0.20$, the pull-off force is -0.64. Compared with the smooth value, the reduction rate, ϕ_r, of the pull-off force is 36%. When $\sigma_S = 0.4$, the pull-off force reduces to 0.18 and the reduction rate is $\phi_r = 82\%$. When $\sigma_S = 1.0$, the pull-off force is only 0.03 and the corresponding reduction rate is $\phi_r = 97\%$. The variance of roughness heights, σ_S, is scaled by the intermolecular equilibrium spacing, $\epsilon \approx 4$ Å. Therefore, $\sigma_S = 1.0$ corresponds to a very small distance of approximately 4 Å. In reality, submicrometer or nanometer roughness can easily exceed this value. As a result, the pull-off force can easily be reduced by 97% when Tabor's parameter value is small. Surface roughness also causes the shift of the approach of pull-off. For a smooth surface, the pull-off force occurs at $\lambda_p = 0$. When small roughness is considered, e.g., $\sigma_S = 0.2$, the pull-off force appears at $\lambda_p = -0.42$. The approach distance of the pull-off force decreases with increasing roughness. For an even higher surface roughness, e.g., $\sigma_S = 1.0$, the net external load reaches the pull-off value at $\lambda_p = -5.78$. In a dimensional measure, the approach for the pull-off force decreases about $5.78\epsilon \approx 23.1$ Å when $\sigma_S = 1.0$. The approach for the equilibrium position also decreases significantly due to surface roughness. For a smooth surface, the approach at the static equilibrium position is $\lambda_e = 0.21$. However, when the surface roughness scale is $\sigma_S = 1.0$, the approach at equilibrium is $\lambda_e = -5.71$. This result indicates that the microparticle deforms more severely if the surface is smooth because of a stronger surface stress and a closer separation between the microparticle and the barrier. Microparticles with rough surfaces deform less compared with those with smooth surfaces. The results also show that the difference between approach distances of pull-off and equilibrium is very small both for the smooth and rough surfaces. In the case of $\sigma_S = 1.0$, $\lambda_p - \lambda_e \approx 0.07$, which is about 0.28 Å.

Figure 14 shows the case for a larger Tabor parameter value of $\mu = 2.0$. It clearly reveals that surface roughness also has significant effects on contact for larger Tabor parameter values. The effects of surface roughness on the pull-off force and the approach for pull-off force are similar to the cases of small Tabor parameter values. The pull-off force is significantly reduced, and the approach at which the pull-off force occurs decreases. For a smooth surface the pull-off force is $F_p = -0.79$ at $\lambda_p = -1.66$. When the surface is rough, i.e., $\sigma_S = 0.2$, the pull-off force reduces to $F_p = -0.52$ with a reduction rate of 34% at $\lambda_p = -1.71$. When $\sigma_S = 0.4$, the pull-off force is $F_p = -0.167$ at $\lambda_p = -2.31$ and the reduction rate is 79%. For $\sigma_S = 1.0$, the pull-off force is -0.03 at $\lambda_p = -5.91$ and the reduction rate is 96%.

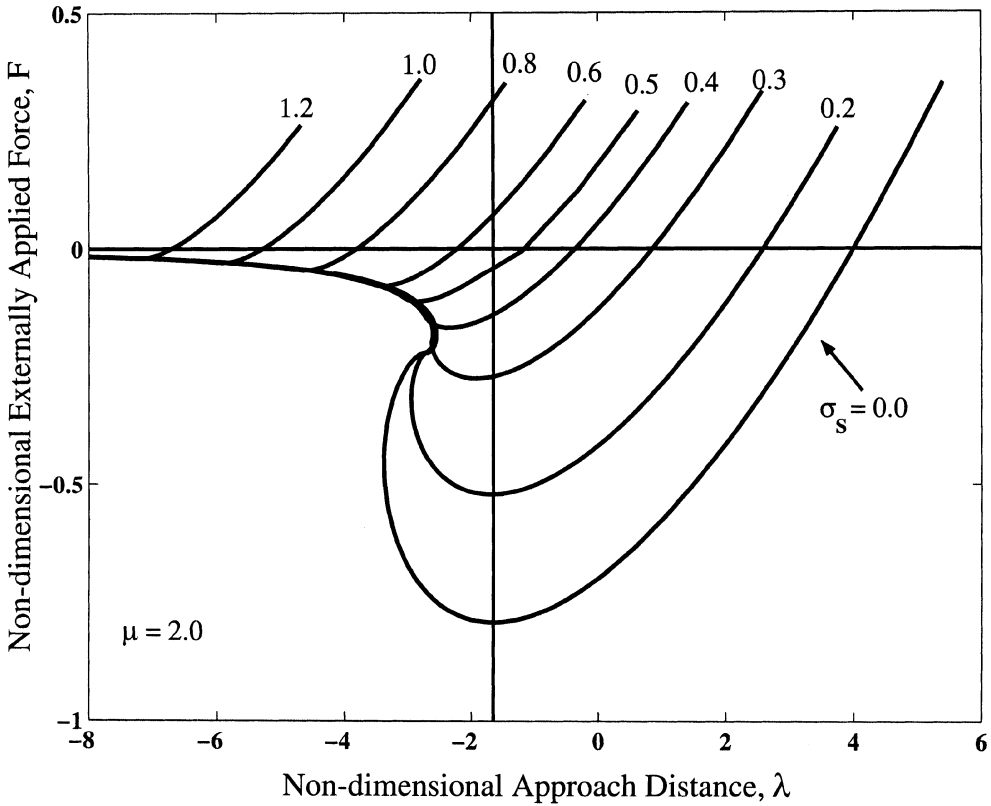

FIGURE 14 Load-approach curves for $\mu = 2.0$.

Figure 14 also shows some features related particularly to large Tabor parameter values. The snap-on and snap-off are the results of strong intermolecular attractions. Surface roughness severely reduces intermolecular adhesion because of the large gaps formed by the roughness heights. The scale and existence of the snap-on and snap-off are changed by surface roughness. Figure 14 shows that the snap-on and snap-off exist only for relatively smooth surfaces in which $0 \leq \sigma_S < 0.4$. The range of the unstable branch, however, is shortened by surface roughness. Snap-on and snap-off disappear when $\sigma_S \geq 0.4$. This can be illustrated by some of the computational results. When $\sigma_S = 0.0$ (a smooth surface), the snap-on happens at $\lambda_a = -2.55$. The corresponding external load is $F_a = -1.82$. The snap-off happens at $\lambda_b = -3.38$ and the corresponding external load is $F_b = -4.54$. The range of the unstable branch is $-3.38 \leq \lambda \leq -2.55$. When $\sigma_S = 0.2$, the snap-on point is $\lambda_a = -2.58$ and the snap-off point is $\lambda_b = -2.95$. The external loads are -1.80 and -3.17 for the snap-on and snap-off, respectively. The range of the unstable branch decreases to the interval of $-2.95 \leq \lambda \leq -2.58$. In other words, the snap-on and the snap-off points are closer. It is also observed that surface roughness decreases the approach for snap-on and snap-off. The change of the status of snap-on and snap-off is confirmed by the case of a higher roughness level. For $\sigma_S = 0.3$, $\lambda_a = -2.61$ and $\lambda_b = 2.63$. The external force at snap-on and snap-off is -1.79 and -2.01, respectively. The snap-on and snap-off points are even closer because the interval for the unstable branch is $-2.63 \leq \lambda \leq -2.61$. A critical state is reached when the snap-on and snap-off points are the same. The variance of roughness height that leads to this critical state can be found through refined simulations by changing the value of σ_S in very fine steps. When $\sigma_S = 0.4$, no snap-on and snap-off points are found. The load-approach curves in Figure 14 also demonstrate the shift of the equilibrium approach due to surface roughness when the value of Tabor's parameter is large. The equilibrium approach values are $\lambda_e = 4.00$, 2.59, -0.364, and -5.28 for $\sigma_S = 0$, 0.2, 0.4, and 1.0, respectively. It is clear that the equilibrium approach decreases significantly as the variance of roughness heights increases.

The effects of roughness can be understood further by analyzing the mean separation and effective stress profiles of the microparticle associated with the pull-off, the snap-on, and snap-off, and the static equilibrium states. Figure 15 shows the separation and surface stress profiles at pull-off for $\mu = 2.0$ with different variances of roughness heights. For relatively smooth surfaces ($\sigma_S \leq 0.4$), the microparticle deforms mainly over the local region near $r = 0$. The outer region is affected less. Because of the strong surface stress and elastic

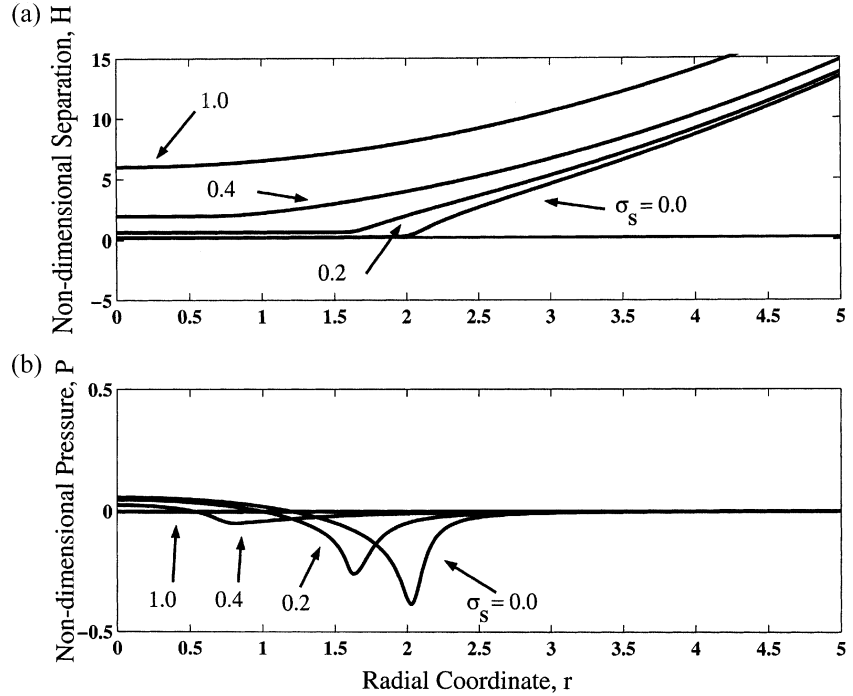

FIGURE 15 Mean profiles of separation and surface stress at pull-off for $\mu = 2.0$ with $\sigma_S = 0.0, 0.2, 0.4$, and 1.0.

deformation, the separation profile over the deformed region is relatively flat. The surface stress decays in the outside region because of the large separation between the microparticle and the barrier. Therefore, the separation over the less affected region still follows the shape of the microparticle. For a high roughness case, e.g., $\sigma_S = 1.0$, the microparticle is basically undeformed at pull-off. The contact region is extremely small. The deformed region shrinks as surface roughness increases. The scope of the deformed region is within $r \leq 3.0$, 2.5, 2.0, and 0.5 for $\sigma_S = 0.0$, 0.2, 0.4, and 1.0, respectively.

The scale of the deformation of the microparticle at pull-off also reduces severely as surface roughness increases. This can be shown by the increase of the separation at $r = 0$. For all cases, the smallest separation occurs at $r = 0$. It is the closest point between the microparticle and the barrier in an average manner. Figure 15 shows that the mean separations at $r = 0$ are -0.009, 0.419, 1.760, and 5.902 for $\sigma_S = 0$, 0.2, 0.4, and 1.0, respectively. The increase of the mean

separation at $r = 0$ is evident as the surface roughness increases. The gap at the pull-off position between the mean datum plane of the microparticle and the barrier is larger if the surface is rough.

As separation changes, surface stress at pull-off changes accordingly. Figure 15 also shows that the approximate compression regions are within $r \leq 1.19$, 0.99, 0.52, and 0.0 for $\sigma_S = 0.0$, 0.2, 0.4, and 1.0, respectively. The compression region is reduced as surface roughness increases. When the variance of roughness is relatively large, e.g., $\sigma_S = 1.0$, there is no compression region. A very small attractive stress distributes over the whole surface and the microparticle is barely deformed. As the compression region shrinks, the peak of the repulsive pressure also decreases. When $\sigma_S = 1.0$, there is no repulsive stress and the peak of the repulsive stress is 0.0554, 0.0466, and 0.0250 for $\sigma_S = 0.0$, 0.2, and 0.4, respectively. For a smooth surface, a positive separation corresponds to an attractive surface stress according to the Lennard-Jones law. However, for a rough surface, a positive separation of the mean datum plane still corresponds to a repulsive stress because of averaging over roughness heights. For $\sigma_S = 0.2$ and 0.4, the mean separation at $r = 0$ is positive but the corresponding effective surface stress is repulsive. Because of surface roughness, the distribution of the attractive stress is no longer concentrated on the edge of the contact area. The peak and the slope of the attractive stress decrease dramatically. The peaks of the attractive stress are -0.3837, -0.2582, -0.0493, and -0.0035, located at $r = 2.0233$, 1.6337, 0.8120, and 0.3860 for $\sigma_S = 0.0$, 0.2, 0.4, and 1.0, respectively. The distribution of the attractive stress is smoothed and the attractive region is enlarged, while the magnitude of the attractive stress is very small. For $\sigma_S = 1.0$, the attractive stress does not exceed -0.0035 over the entire contact region.

The mean separation and effective surface stress at the equilibrium position for $\mu = 2.0$ are illustrated in Figure 16. The separations between the mean datum planes at the equilibrium position increase as the surface roughness increases. The lowest separation between the mean datum planes at $r = 0$ are -0.0270, 0.4154, 1.7512, and 5.7412 for $\sigma_S = 0.0$, 0.2, 0.4, and 1.0, respectively. At equilibrium for all values of σ_S, the microparticle deforms significantly at the region around $r = 0$. Consequently, the separation over the deformed region is flattened. The flattened region shrinks as σ_S increases. The ranges of the flattened region are $r \leq 3.39$, 2.81, 1.69, and 0.95 for $\sigma_S = 0.0$, 0.2, 0.4, and 1.0, respectively. The effective attraction and its slope reach a peak value at the edge of the flattened region. The peak of attraction reduces significantly as σ_S increases. The peak of attraction is -0.3223, -0.2583, -0.0493, and -0.0035 for $\sigma_S = 0.0$, 0.2, 0.4, and 1.0,

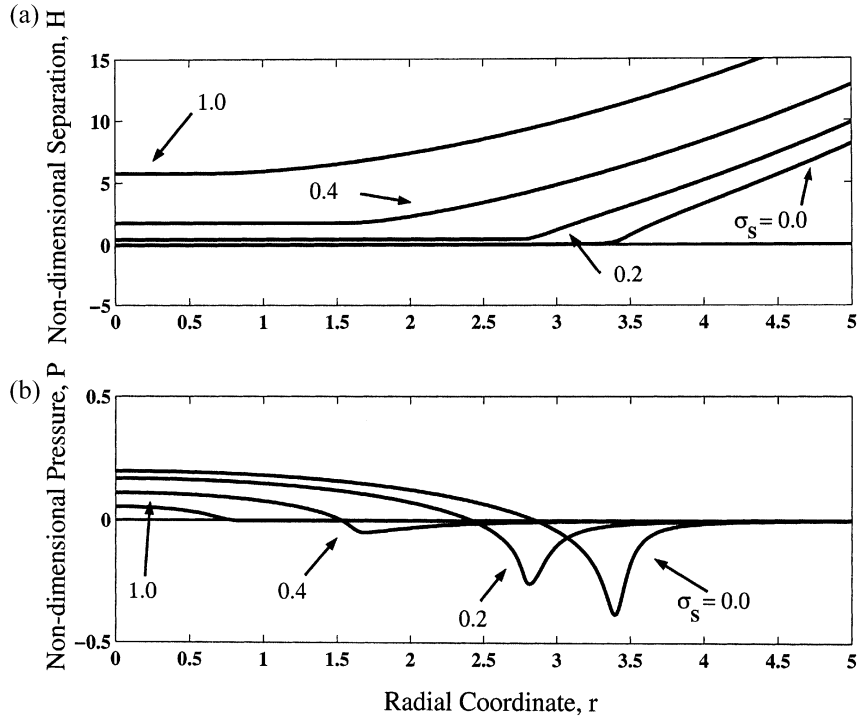

FIGURE 16 Mean profiles of separation and surface stress at equilibrium for $\mu = 2.0$ with $\sigma_S = 0.0, 0.2, 0.4$, and 1.0.

respectively. At the equilibrium position, the repulsion and attraction are balanced so that the net external force vanishes. When σ_S is large, the intensity of the attraction is extremely small. To balance the repulsion the attraction region has to be significantly large. When $\sigma_S \geq 1.0$ the magnitude of the attractive stress is negligible. This stress distribution does not agree with either the DMT or the JKR theory; a Hertzian distribution may be more appropriate.

Figure 17 shows the reduction rates of the pull-off force, ϕ_r, as a function of the variance of roughness heights, σ_S, for different Tabor parameters. It is clear that ϕ_r is quite sensitive to σ_S. The difference of reduction rate for different Tabor parameter values is very small. When $\sigma_S \geq 1.0$, no significant difference in reduction rate is observed as the Tabor parameter value changes. The variance of roughness heights, σ_S, becomes the dominant factor for the reduction rate. There are two regions in the curve. The slope in the interval of $0 \leq \sigma_S \leq 0.4$ is relatively steeper than that of $\sigma > 0.4$. This can be explained by

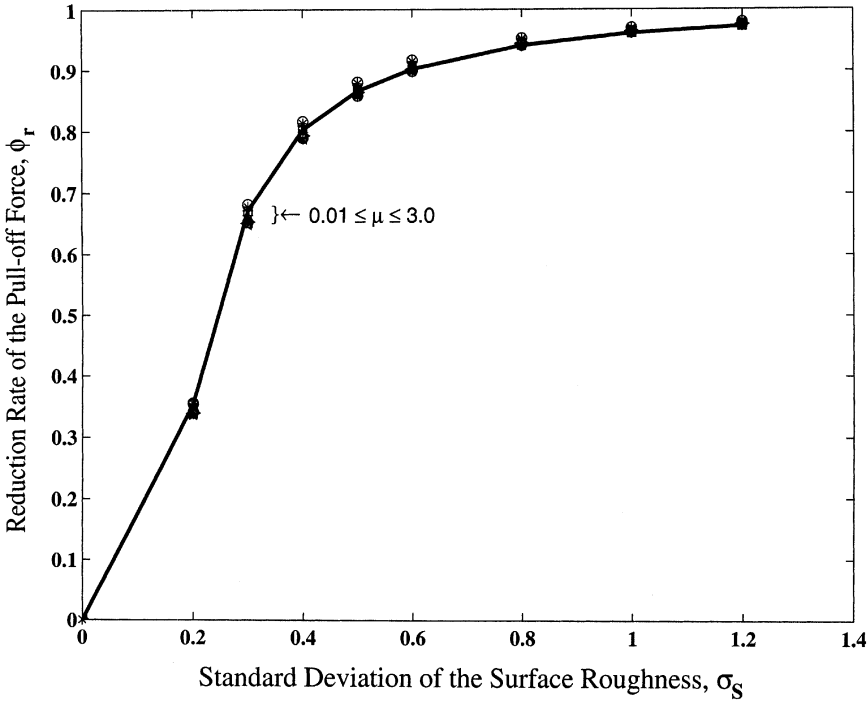

FIGURE 17 Reduction rates of the mean pull-off force, ϕ_r, as a function of the variance of roughness heights, σ_S, for different Tabor parameter values.

the profile of separation shown in Figure 15. When $\sigma_S > 0.4$, the mean datum plane of the microparticle is barely deformed at pull-off. The major interaction between the microparticle and the flat barrier is attraction. According to the Lennard-Jones law, the attraction decays very slowly at large separation. Therefore, a change in the reduction rate is less because of the slow decay rate of attraction for large separations. Results also show that surface roughness has a significant effect on the pull-off force. Even with a very small variance of roughness height, the pull-off force reduces dramatically. The pull-off force reduces about 50% at $\sigma_S = 0.24$ ($\sigma_s = 0.24\epsilon$). For both small and large Tabor parameter values, the reduction rate can easily achieve 95% when $\sigma_S \geq 1.0$ ($\sigma_s \geq \epsilon$). At $\sigma_S = 1.2$, the reduction rate reaches a value of 97%. Further reduction is difficult to achieve with submicrometer-level surface roughness. A larger scale of surface irregularity as discussed previously is needed. Figure 18 shows the pull-off force as a function of the Tabor parameter value for different

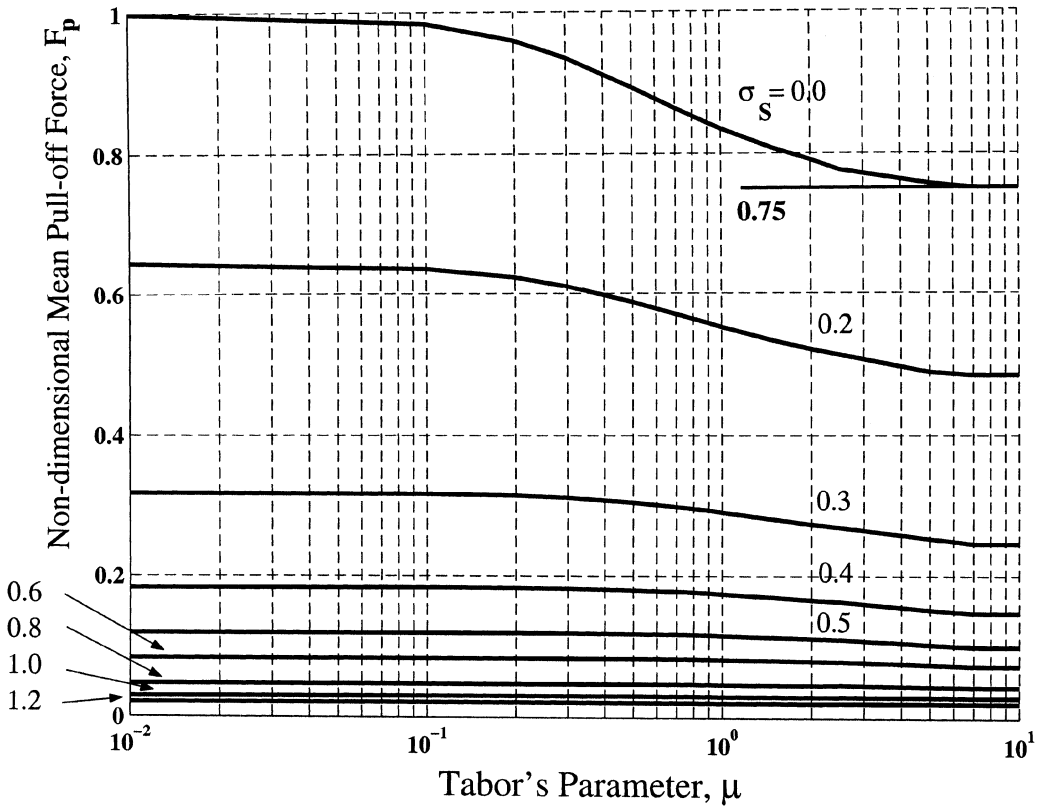

FIGURE 18 The mean pull-off force as a function of Tabor's parameter with different values of σ_S.

values of σ_S. For $\sigma_S = 0.0$, because the same numerical method and theory are used, the results are the same as those of Greenwood [10] and Feng [11]. It reveals a smooth transition from the DMT theory ($F_p = 2\pi R\gamma$) to the JKR theory ($F_p = \frac{3}{2}\pi R\gamma$). The pull-off force decreases at almost the same rate as shown in Figure 17 when σ_S increases. Figure 18 can be used as a map to find the reduced pull-off force for different Tabor parameter values and different surface roughnesses.

Finally, it must be mentioned that the results presented in this paper are based upon statistical averaging over the Gaussian distribution of the roughness height shown in Equation (10). The solution for a specific rough surface is more complicated. Individual asperities cause multiple contacts and, therefore, multiple snap-off, snap-on, and pull-off. The smooth load-approach curve and profiles for separation and surface stress become irregular. The statistical averaging method used in this paper can give more systematic results, which demonstrate the effects that surface roughness has on mean adhesive contact behavior.

CONCLUSIONS

This paper presents a method for investigation of effects of roughness on adhesion for a microparticle in contact with a nominally flat surface over a circular area. The statistical mean load-approach curves, the profiles of the mean separation, and the effective surface stress are computed for a Gaussian gap perturbation. It is found that surface roughness dramatically changes the status of snap-on and snap-off. When the variance of roughness heights is relatively large, snap-on and snap-off can disappear. The separation and stress distributions for very rough surfaces are similar to those predicted by Hertzian theory. Results also reveal that surface roughness significantly reduces the pull-off force. When the surface roughness is large, the variance of roughness heights is the dominant factor in the reduction of the pull-off force. With even a very small variance of roughness height the pull-off force reduces dramatically. Further reduction is difficult to achieve with submicrometer-level surface roughness, implying that a larger scale of surface irregularity may be needed to achieve this. The statistical distribution used in this work was Gaussian (normal); a log-normal distribution may be more realistic. In addition, the statistical variations added to the contact gap were introduced as a small perturbation, and it is not known if the results for large values of the standard deviation are realistic. Although the trends between adhesion force and roughness found in this paper agree with existing measurements, comparisons with experimental measurements for surfaces with controlled random roughness should be carried out.

REFERENCES

[1] Burnham, N. A., Behrand, O. P., Oulevy, F., Gremand, G., Gallo, P.-J., Kulik, A. J., Pollock, H. M., and Briggs, G. A., *Nanotechnology* **8**, 67–75 (1997).
[2] Bradley, R. S., *Phil. Mag.* **13**, 853–862 (1932).
[3] Derjaguin, B. V., *Kolloid Z.* **69**, 155–164 (1934).
[4] Johnson, K. L., Kendall, K., and Roberts, A. D., *Proc. Roy. Soc. London A* **324**, 301–313 (1971).
[5] Derjaguin, B. V., Muller, V. M., and Toporov, Yu. P., *J. Colloid Interface Sci.* **53**, 314–326 (1975).
[6] Tabor, D., *J. Colloid Interface Sci.* **58**, 2–13 (1977).
[7] Muller, V. M., Yushchenko, V. S. and Derjaguin, B. V., *J. Colloid Interface Sci.* **77**, 91–101 (1980).
[8] Maugis, D., *J. Colloid Interface Sci.* **150**, 243–269 (1992).
[9] Attard, P., and Parker, J. L., *Phys. Rev. A* **46**, 7959–7971 (1992).
[10] Greenwood, J. A., *Proc. Roy. Soc. London A* **453**, 1277–1297 (1997).
[11] Feng, J. Q., *Colloids and Surfaces A: Physicochemical and Engineering Aspects* **172**, 175–198 (2000).
[12] Johnson, K. L., and Greenwood, J. A., *J. Colloid Interface Sci.* **192**, 326–333 (1997).
[13] Krupp, H., *Adv. Colloid Interface Sci.* **1**, 111 (1967).
[14] Sharpe, L. H., *J. Adhesion* **6**, 13–21 (1974).
[15] Johnson, K. L., *Tribology International* **31**, 413–418 (1998).
[16] Fuller, K. N. G., and Tabor, D., *Proc. Roy. Soc. London A* **345**, 327–342 (1975).
[17] Schaefer, D. M., Carpenter, M., Reifenberger, R., Demejo, L. P., and Rimai, D. S., *J. Adhesion Sci. and Technol.* **8**, 197–210 (1994).
[18] Mizes, H. A., *J. Adhesion Sci. Technol.* **8**, 937–951 (1994).
[19] Briscoe, B. J., Liu, K. K., and Williams, D. R., *J. Colloid Interface Sci.* **200**, 256–264 (1998).
[20] Rabinovich, Y. I., Adler, J. J., Ata, A., Singh, R. K., and Moudgil, B. M., *J. Colloid and Interface Sci.* **232**, 17–24 (2000).
[21] Reeks, M. W., Reed, J., and Hall, D., *J. Phys., D: Appl. Phys.* **21**, 574–589 (1988).
[22] Soltani, M., and Ahmadi, G., *J. Adhesion* **51**, 105–123 (1995).
[23] Ingham, D. B., and Yan, B., *J. Aerosol Sci.* **25**, 327–340 (1994).
[24] Ziskind, G., Fichman, M., and Gutfinger, C., *Aerosol Sci. Technol.* **28**, 623–634 (1997).
[25] Greenwood, J. A., and Tripp, J. H., *Trans. ASME J. Applied Mechanics* **341**, 153–159 (1967).
[26] Majumdar, A., and Bhushan, B., *J. Tribology* **112**, 205–216 (1990).
[27] Greenwood, J. A., and Williamson, J. B. P., *Proc. Roy. Soc. London A* **295**, 300–319 (1966).
[28] Greenwood, J. A., *Trans. ASME J. Lub. Tech.* **89**, 81–91 (1966).
[29] Johnson, K. L., *Contact Mechanics* (Cambridge University Press, Cambridge, UK, 1985), pp. 76–77.
[30] Abramowitz, M., and Stegun, I. A., *Handbook of Mathematical Functions With Formulas, Graphs, and Mathematical Tables* (National Bureau of Standards, Applied Mathematics Series, Washington DC, USA, 1967) **55**, Sixth Printing, p. 924, Table 25.10.
[31] Press, W. H., Teukolsky, S. A., Vetterling, W. T., and Flannery, B. P., *Numerical Recipes* (Cambridge University Press, Cambridge, 1992), 2nd. ed.
[32] Keller, H. B., *Lectures on Numerical Methods in Bifurcation Problems* (Springer-Verlag, New York, 1987).